Supporting Information on

Heteroaggregation behavior of graphene oxide on Zr-based metal−organic frameworks in aqueous solutions: a combined experimental and theoretical study

Jie Li,[a, b] Qunyan Wu,[c] Xiangxue Wang,[a] Zhifang Chai,[c, d] Weiqun Shi,[c,*] Jing Hou,[a] Tasawar Hayat,[e] Ahmed Alsaedi[e] and Xiangke Wang[a, d, e,*]

[a]College of Environmental Science and Engineering, North China Electric Power University, Beijing, 102206, P. R. China

[b]School of Resources and Environment, Anhui Agricultural University, Hefei, 230036, P. R. China

[c]Laboratory of Nuclear Energy Chemistry and Key Laboratory for Biomedical Effects of Nanomaterials and Nanosafety, Institute of High Energy Physics, Chinese Academy of Sciences, Beijing, 100049, P. R. China

[d]Collaborative Innovation Center of Radiation Medicine of Jiangsu Higher Education Institutions and School for Radiological and Interdisciplinary Sciences, Soochow University, 215123, Suzhou, P. R. China

[e]NAAM Research Group, Faculty of Science, King Abdulaziz University, Jeddah, 21589, Saudi Arabia

Preparation of GO

GO was prepared by using the modified Hummers method from the flake graphite (average particle diameter of 20 mm, 99.95 % purity, Qingdao Tianhe Graphite Co.

Ltd., China). Briefly, 1.0 g of graphite, 0.5 g of $NaNO_3$, and 23 mL of H_2SO_4 were mixed and stirred in a three neck flask in an acid bath, and then, 3.0 g of $KMnO_4$ was slowly added. Once added, the solution was transferred to a 35 ± 1 °C water bath and stirred for about 3 h; then, 40 mL Milli-Q water was added; after that the solution was stirred for 30 min at temperature of 95 ± 1 °C. Then, 140 mL Milli-Q water was added and 3 mL of H_2O_2 (30 %) was added slowly, turning the color of the solution from dark brown to yellow. The warm solution was filtered and rinsed with 300 mL 10 % of HCl solution. The GO solution was obtained and then rinsed it until the solution pH > 4.0.

Preparation of Zr-based MOFs

All Zr-based MOFs, including UiO-66, UiO-66-NH_2, UiO-66-OH, UiO-66-$(OH)_2$, and UiO-67, were synthesized using the following general procedure and the amounts of reagents listed in Table S1. An 8-dram vial was loaded with $ZrCl_4$, one third of the DMF, and concentrated HCl before being sonicated for 20 minutes until fully dissolved. The ligand and the remainder of the DMF were then added and the mixture was sonicated for an additional 20 minutes before being heated at 80 °C overnight (BPDC was not completely soluble under these conditions). The resulting solid was then filtered over a fine frit and washed first with DMF (2×30 mL) and then with EtOH (2×30 mL). The sample was filtered for several hours to remove all residual solvent.

Characterization of GO and Zr-based MOFs

Scanning electron microscopy (SEM) images were performed using Hitachi S4800 field emission scanning electron microscopy at 10 kV. Transmission electron microscopy (TEM) images were observed on a FEI Tecnai G2 F20 electron microscope

operated at 200 kV with the software package for automated electron tomography. Powder X-ray diffraction (XRD) patterns were obtained on a Panaltical X'Pert-pro MPD X-ray power diffract meter by using Cu Ka radiation (λ = 1.54056 Å). Fourier transformed infrared (FTIR) spectra were performed on a Nicolet Magana-IR 750 spectrometer over a range from 400 to 4000 cm-1. The Brunauer-Emmett-Teller (BET) surface area was measured from N_2 adsorption-desorption isotherms obtained using a Micromeritics ASAP 2010 at 77 K. The zeta potential values of GO and Zr-based MOFs suspension at different pH values were performed using a Zeta Potential Analyzer (Brookhaven instrument Corp., Holtsville, New York). Atomic force microscopy images (AFM) were determined using atomic force microscopy (AFM, Agilent 5400).

Computational calculation

All structures were optimized using the hybrid exchange-correlation function B3LYP method with the Gaussian 09 program. The quasi-relativistic pseudo-potential ECP28MWB and associated ECP28MWB valence basis sets were used to describe Zr atom, the 6-31G(d) basis set was used for the other light atoms H, C and O.
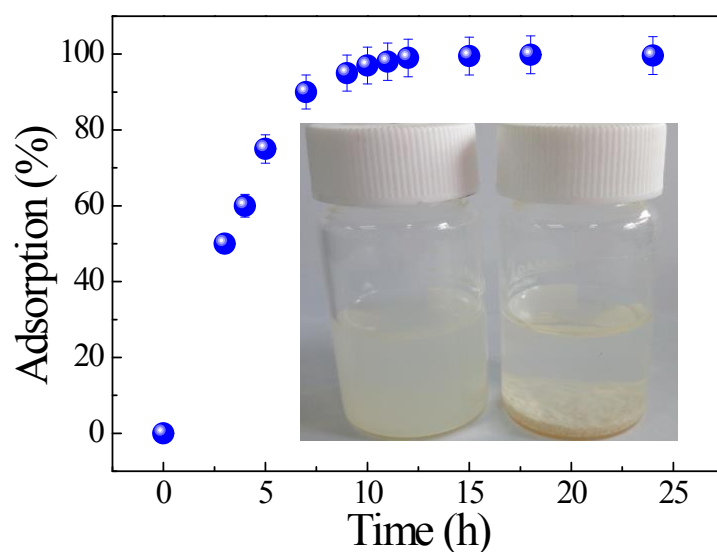
Fig. S1 Adsorption of GO by UiO-66 as a function of adsorption time. It is shown that the adsorption could reach equilibrium after 12 h. Therefore, we chose 24 h as the equilibration time for achieving adsorption completion in the adsorption-desorption experiments. The inserted picture was the digital photo of GO−UiO-66 mixture before (Left) and after (Right) settling for 6 h, which means that the Zr-based MOFs could be separated from GO suspension after settlement for 6 h.
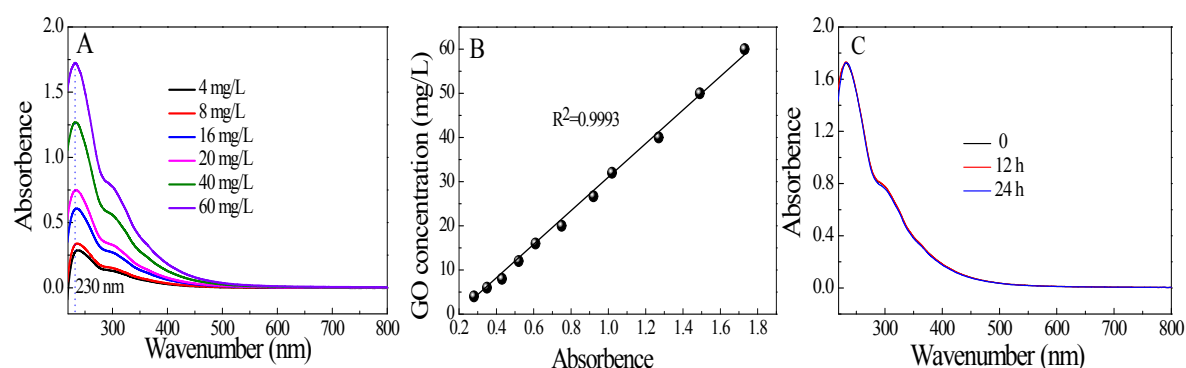

Fig. S2 UV-Vis absorption spectra of GO (A) and the standard curve of GO at an absorbance of 230 nm (B). GO sheets showed a characteristic peak at 230 nm due to the $\pi \rightarrow \pi^*$ transition of the C=C bonds. The standard curve had an R^2 value of 0.9993. So GO concentrations in the supernatants were determined at 230 nm using a UV−Vis spectrophotometer. UV-Vis absorption spectra of GO solution (60 mg/L) in the absence of Zr-MOFs after settlement for different aging time (C).
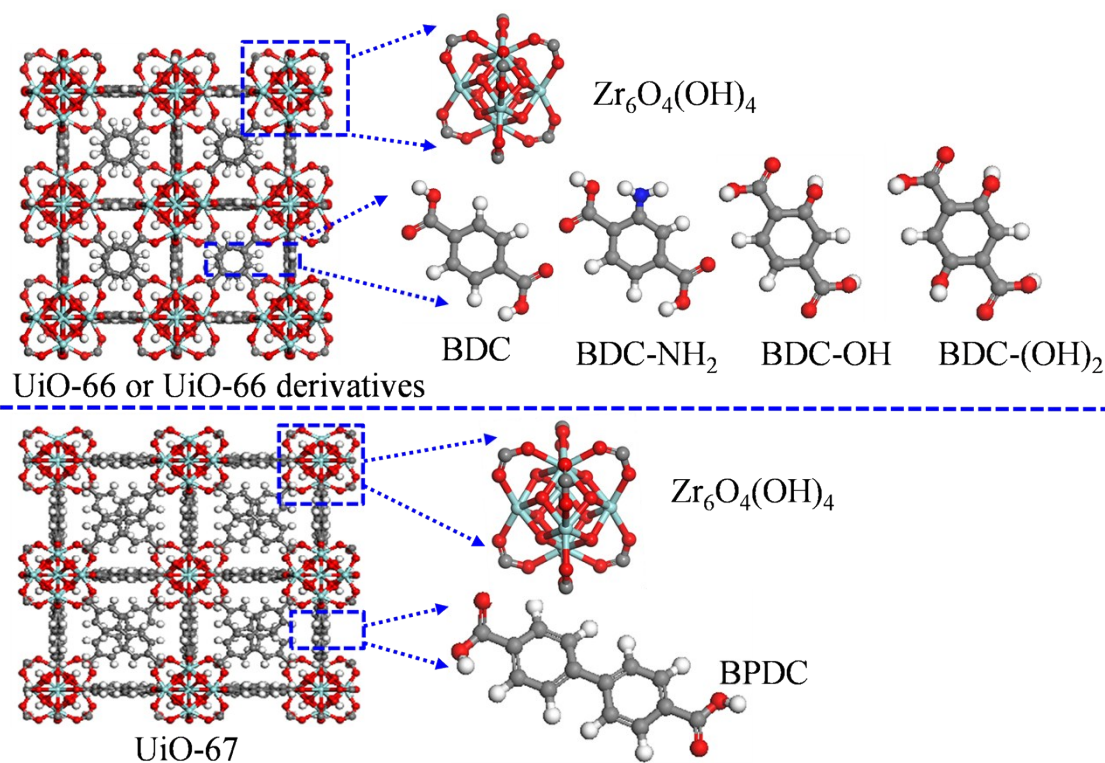
Fig. S3 Structure of UiO-66, UiO-66 derivatives and UiO-67. UiO-66 and UiO-67 were employed to investigate how the heteroaggregation may be affected by the geometric dimensions with different organic linkers. UiO-66 derivatives consisting of BDC linkers functionalized with −NH$_2$ and −OH were also employed to investigate how the aggregation and removal behavior may be influenced by the existence of different functional groups on the organic structures.
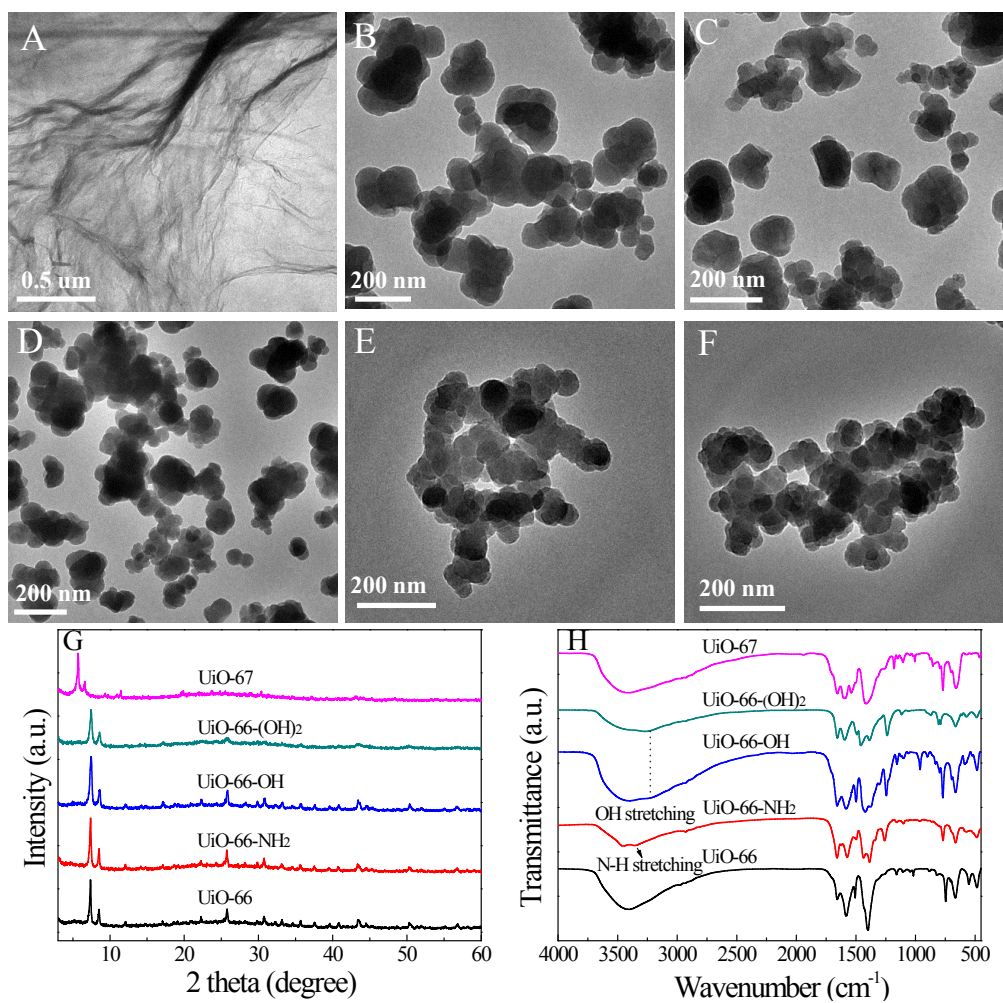
Fig. S4 TEM images of GO (A), UiO-66 (B), UiO-66-NH$_2$ (C), UiO-66-OH (D), UiO-66-(OH)$_2$ (E) and UiO-67 (F); XRD patterns of the Zr-based MOFs (G); and FTIR spectra of the Zr-based MOFs (H).
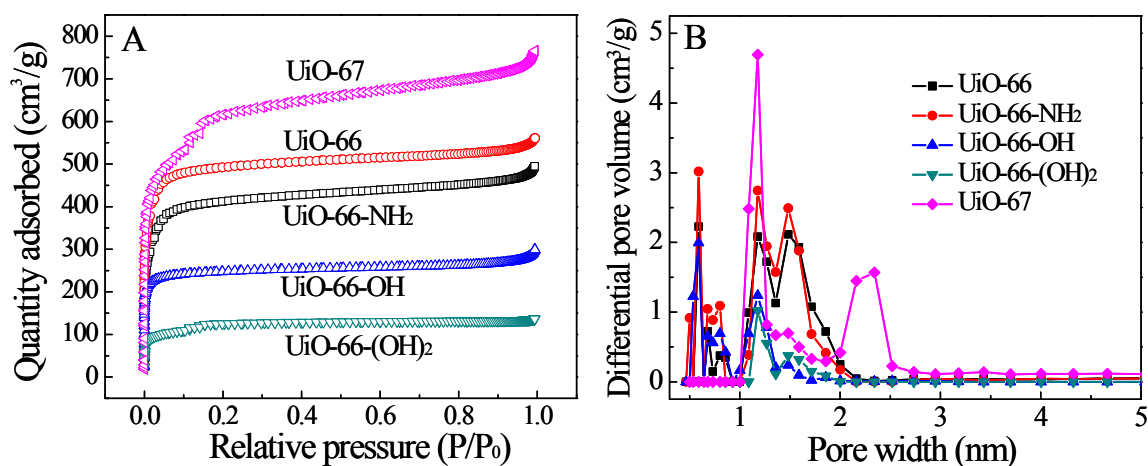
Fig. S5 N_2 adsorption isotherms (A) and the pore size distributions (B) of Zr-based MOFs.
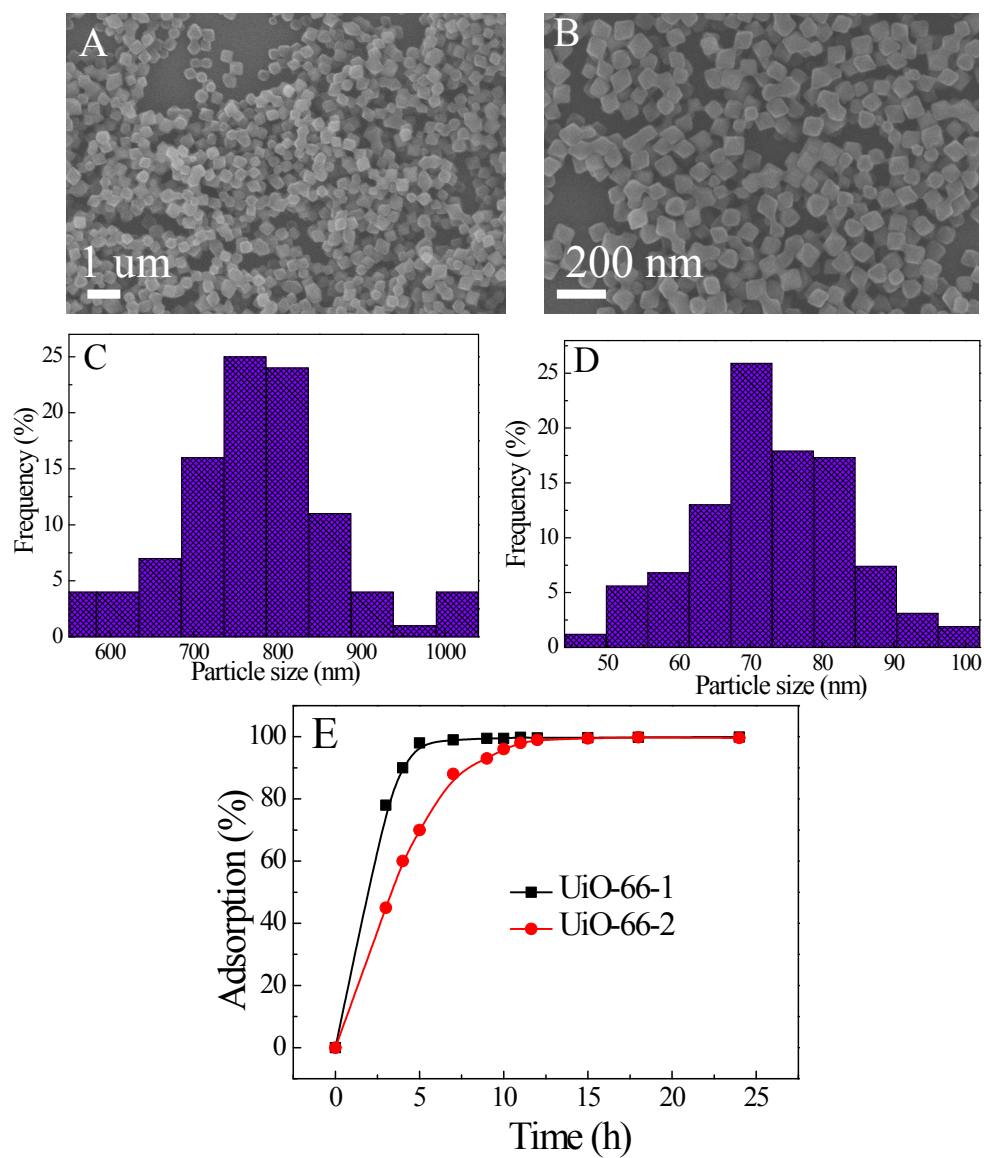

Fig. S6 SEM images of UiO-66-1 (A) and UiO-66-2 (B); corresponding particle size distribution of UiO-66-1 (C) and UiO-66-2 (D); and adsorption of GO by UiO-66-1 and UiO-66-2 as a function of adsorption time (E).
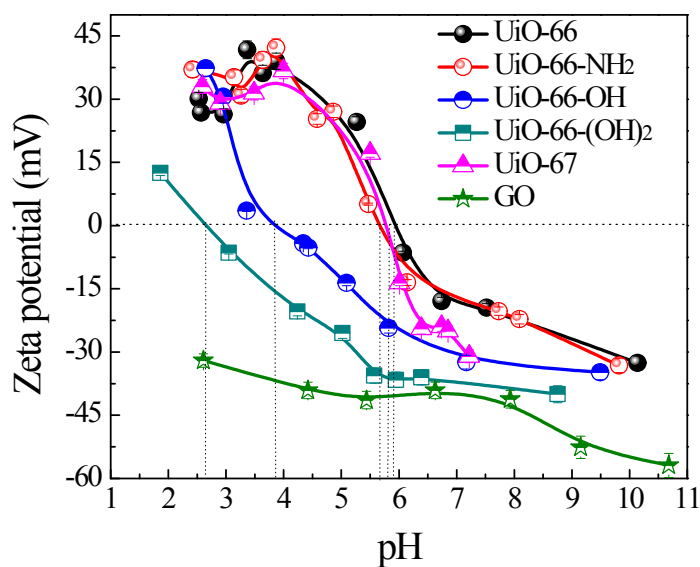
Fig. S7 Zeta potentials of Zr-based MOFs and GO as a function of solution pH. In the experimental pH range of 2.6 to 9.6, GO sheets were highly negatively charged with the surface charges lower than −30 mV, suggesting that the high surface charges of GO sheets are the main cause for the stable GO suspension. There are two inflection points at pH about 4.3 and 8.1 on the pH−zeta potential curve of GO. Ionization of different acidic groups can be responsible for the increase of negative charges on GO sheets. Two kinds of acidic groups including carboxylic (pKa=4.3) and phenolic hydroxyl groups (pKa=9.8) locate on GO sheets, which can account for the observed curve shape.
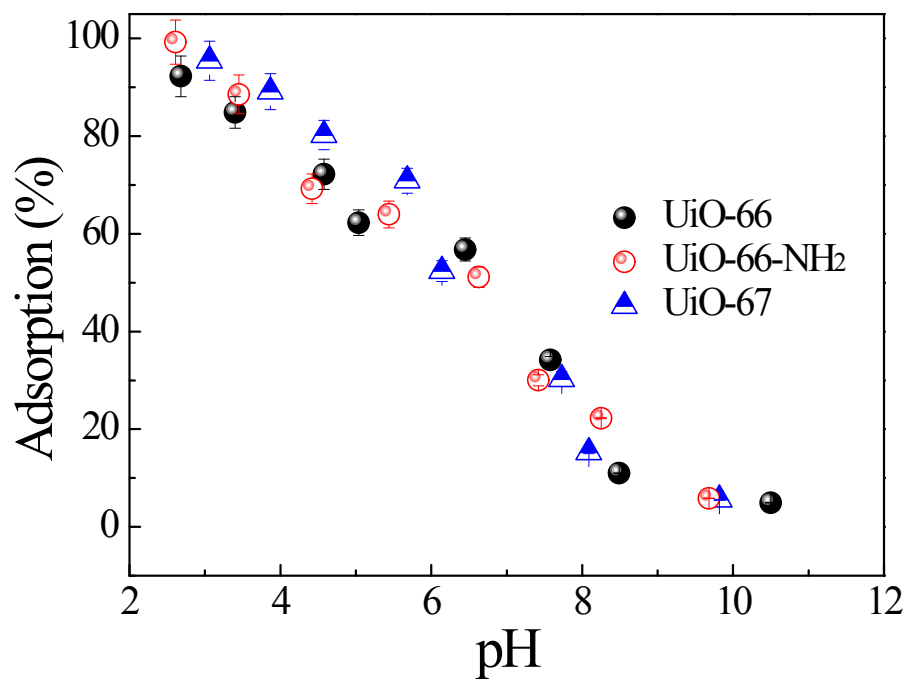
Fig. S8 Adsorption of GO on UiO-66, UiO-66-NH$_2$ or UiO-67 as a function of solution pH.

Fig. S9 Digital pictures of GO−Zr-based MOF heteroaggregates in the binary system (A-C). TEM image of GO−UiO-66 heteroaggregates (D); TEM image of GO−UiO-66-NH$_2$ heteroaggregates (E); TEM image of GO−UiO-67 heteroaggregates (F). XRD patterns of the GO−Zr-based MOF heteroaggregates in the binary system (G); and FTIR spectra of GO and the GO−Zr-based MOF heteroaggregates in the binary system (H).

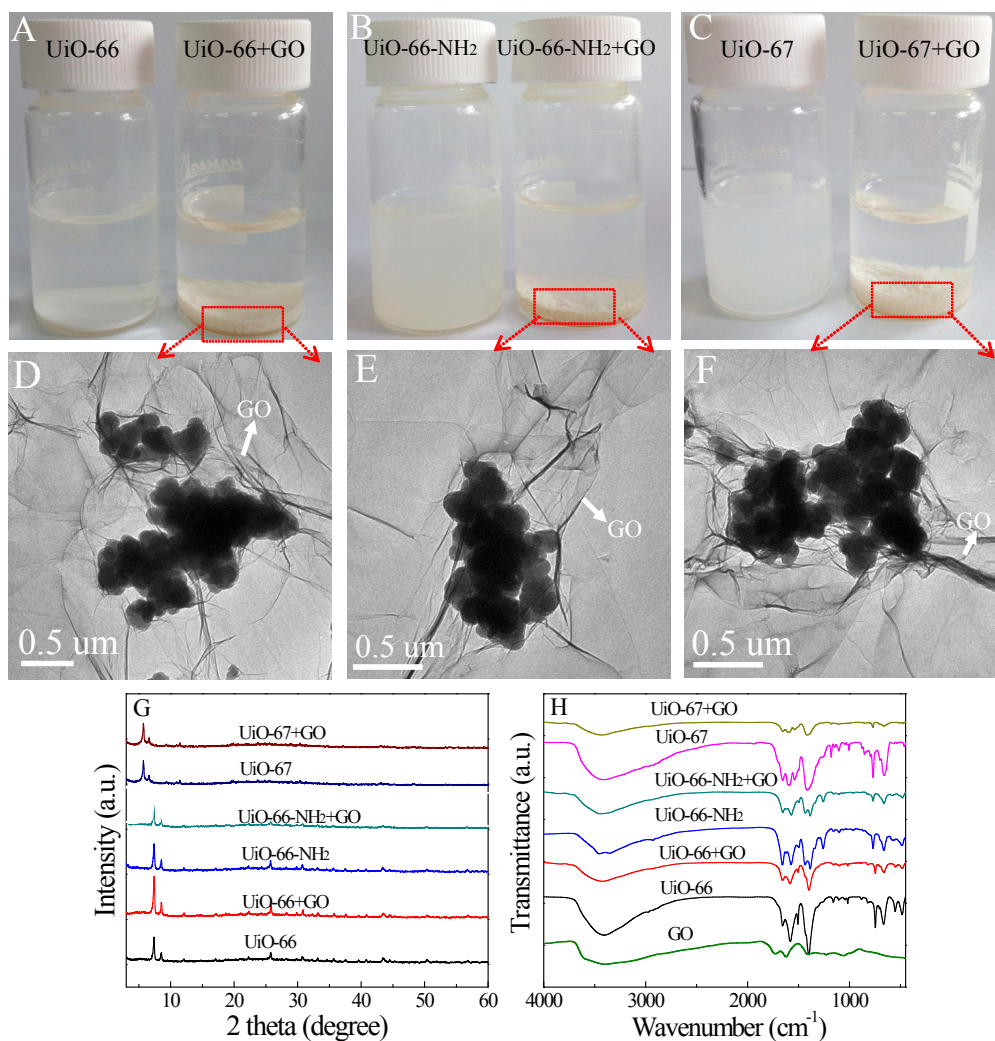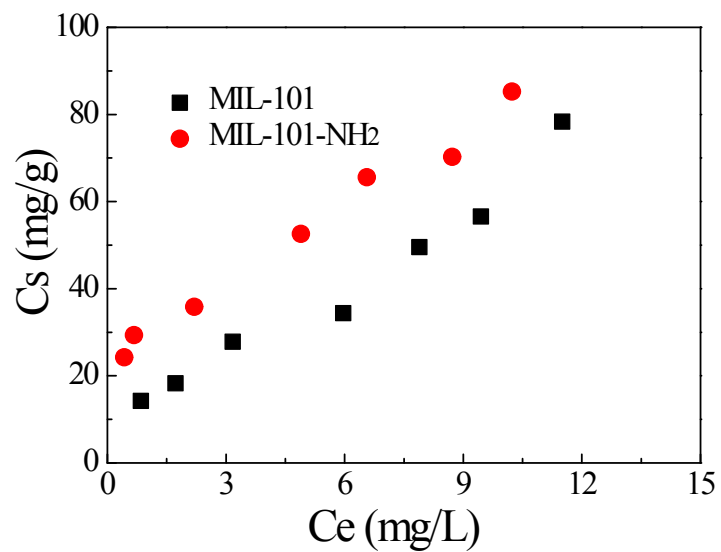**Fig. S10** Heteroaggregation kinetics of MIL-101 and MIL-101-NH$_2$ with GO.
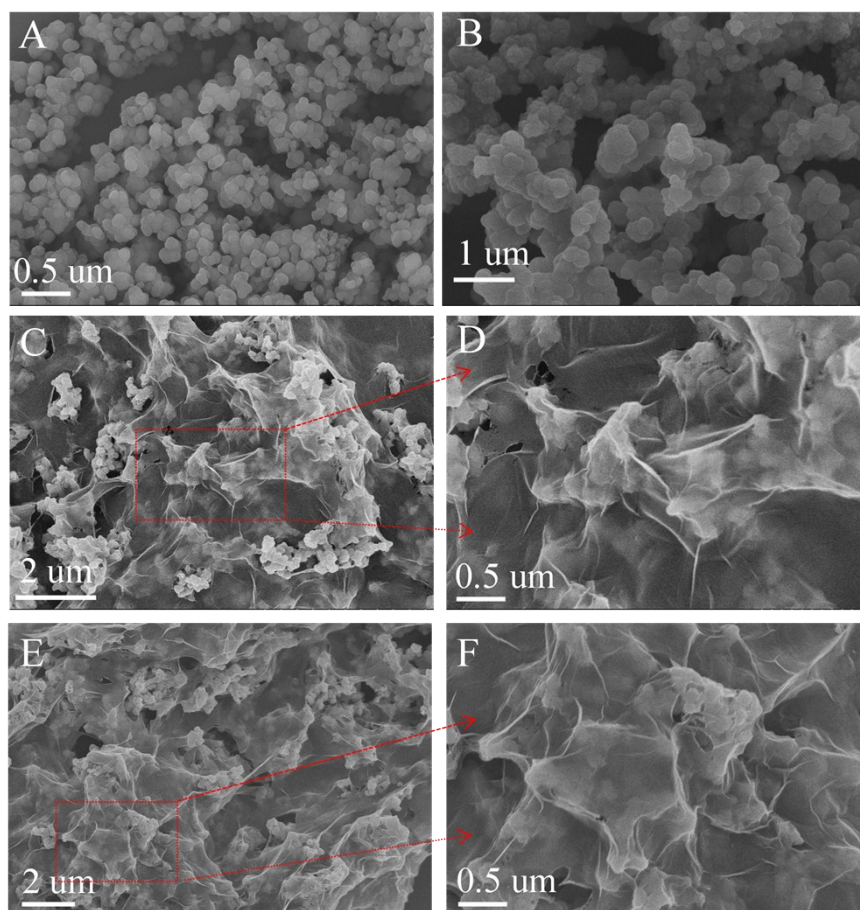
Fig. S11 GO−Zr-based MOF heteroaggregates in the binary system. SEM image of

UiO-66 (A); SEM image of UiO-66-NH$_2$ (B); SEM image of GO−UiO-66

heteroaggregates (C); and SEM image of UiO-66-NH$_2$ heteroaggregates (E). The

images in panels D and F are enlarged from panel C and E.
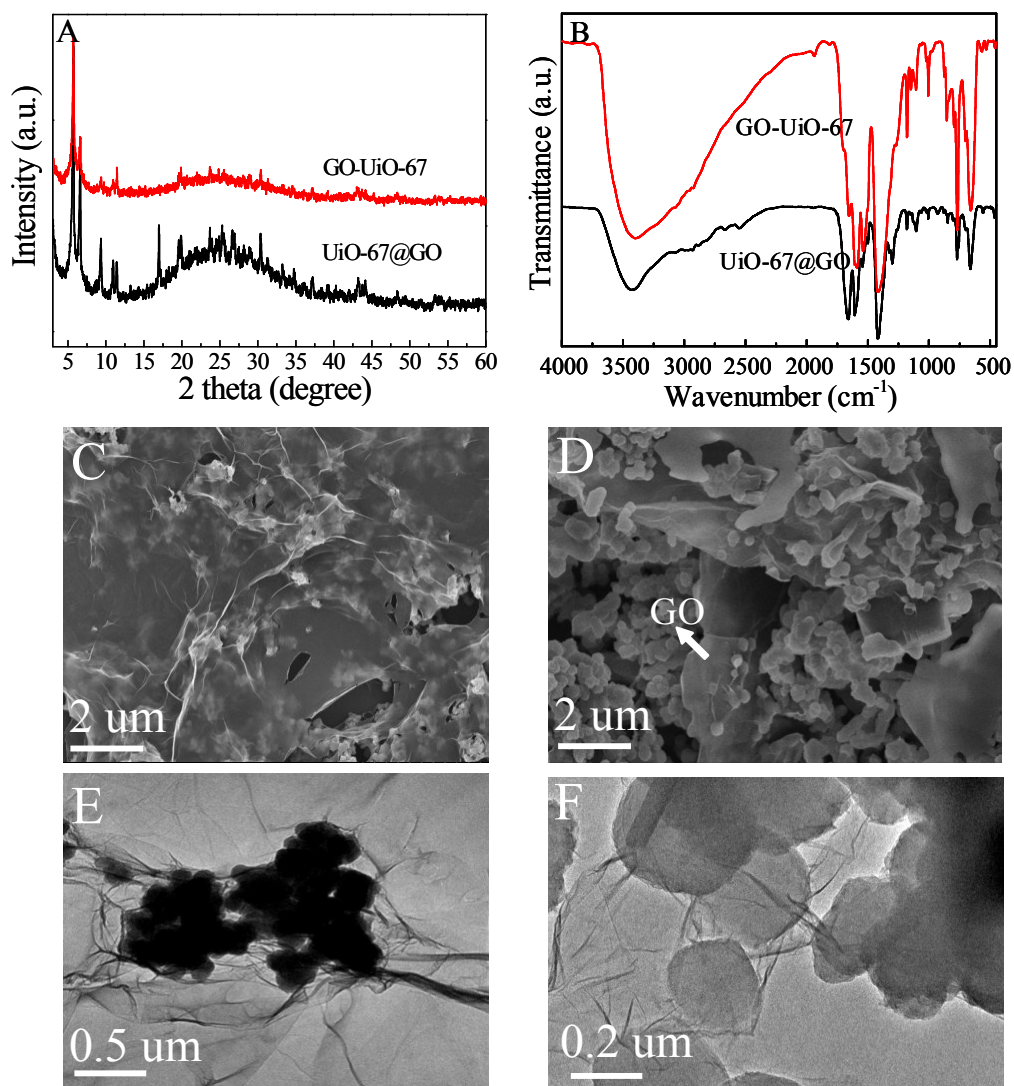
Fig. S12 Comparison between GO−UiO-67 heteroaggregates in the binary system and in situ growth of UiO-67 particles on the GO sheets. XRD patterns (A); FTIR spectra (B); SEM image of GO−UiO-67 (C); TEM image of GO−UiO-67 (D); SEM image of UiO-67@GO (E); and TEM image of UiO-67@GO (F).
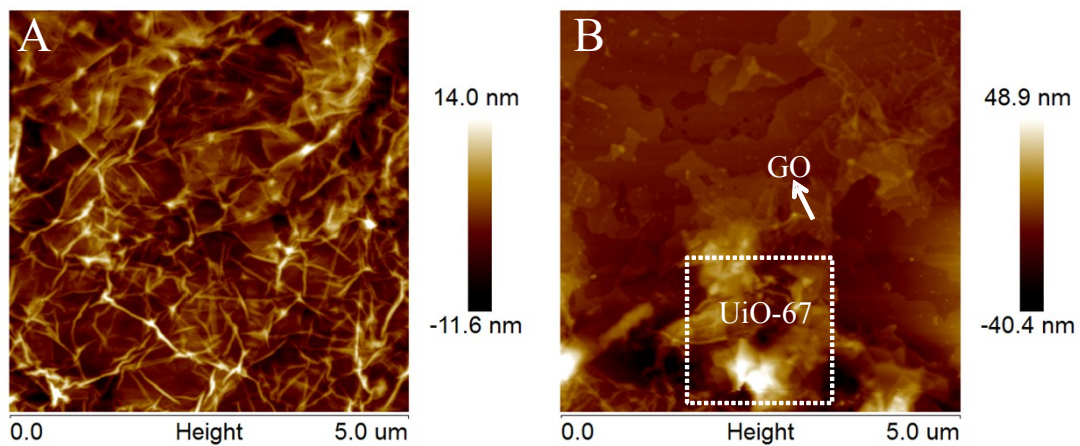
Fig. S13 AFM images of GO (A) and GO−UiO-67 heteroaggregates (B).
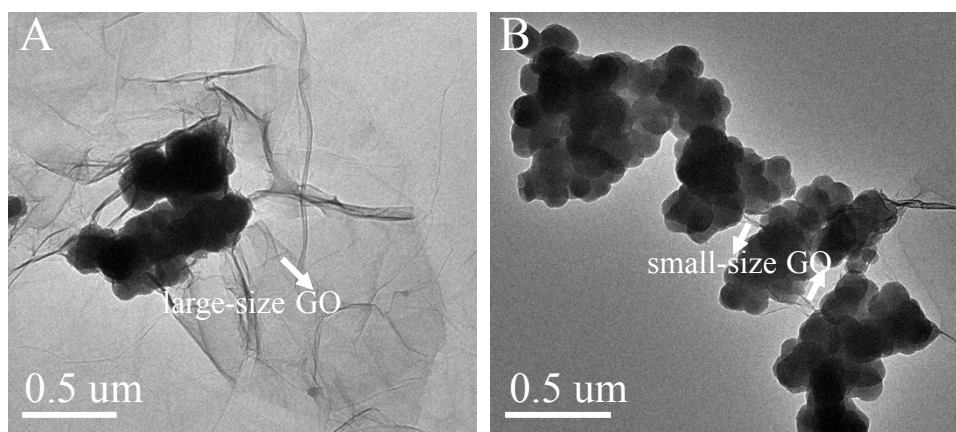
Fig. S14 TEM images of UiO-67 aggregation with large-size GO (A) and small-size GO (B).

UiO-66+GO-1, 0.0　　　UiO-66+GO-2, 0.34　　　UiO-66+GO-3, 0.39　　　UiO-66+GO-4, 0.40

UiO-66+GO-5, 0.48　　　UiO-66+GO-6, 0.52　　　UiO-66+GO-7, 0.55　　　UiO-66+GO-8, 0.56

UiO-66+GO-9, 0.59　　　UiO-66+GO-10, 0.62　　　UiO-66+GO-11, 0.62　　　UiO-66+GO-12, 0.83
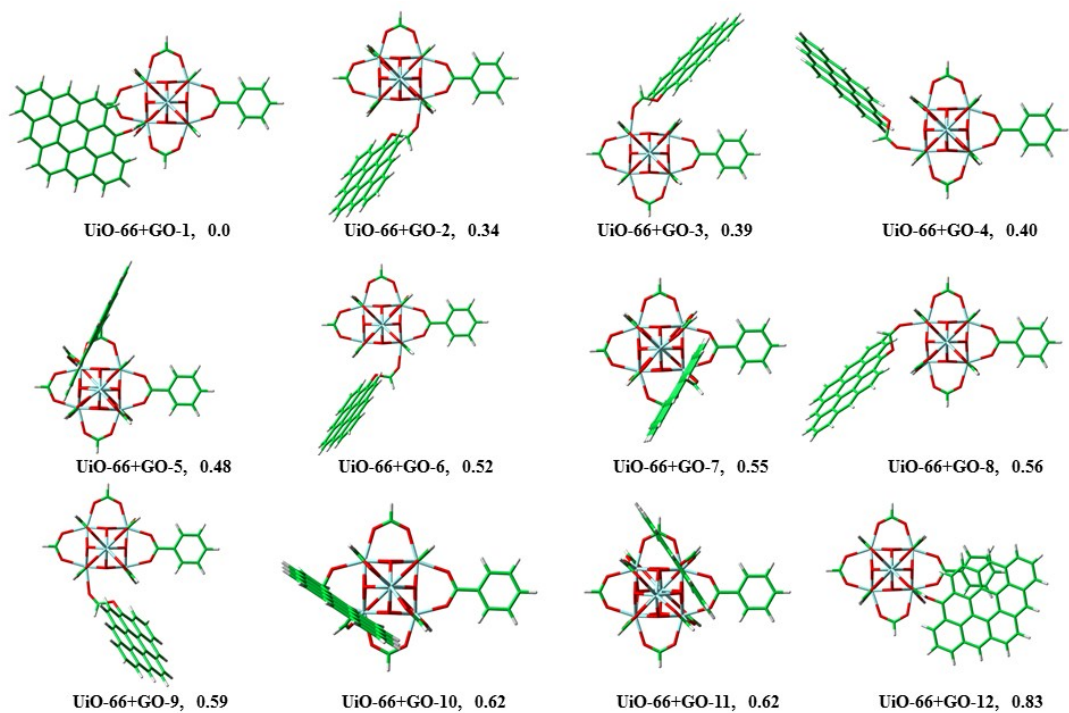
Fig. S15 Optimized adsorption structures of UiO-66 toward GO, the relative energies are provided (kcal/mol).

UiO-66-OH+GO-1, 0.0　　　UiO-66-OH+GO-2, 0.18　　　UiO-66-OH+GO-3, 0.26　　　UiO-66-OH+GO-4, 0.36

UiO-66-OH+GO-5, 0.41　　　UiO-66-OH+GO-6, 0.42　　　UiO-66-OH+GO-7, 0.48　　　UiO-66-OH+GO-8, 0.54

UiO-66-OH+GO-9, 0.57　　　UiO-66-OH+GO-10, 0.60　　　UiO-66-OH+GO-11, 0.60　　　UiO-66-OH+GO-12, 0.61
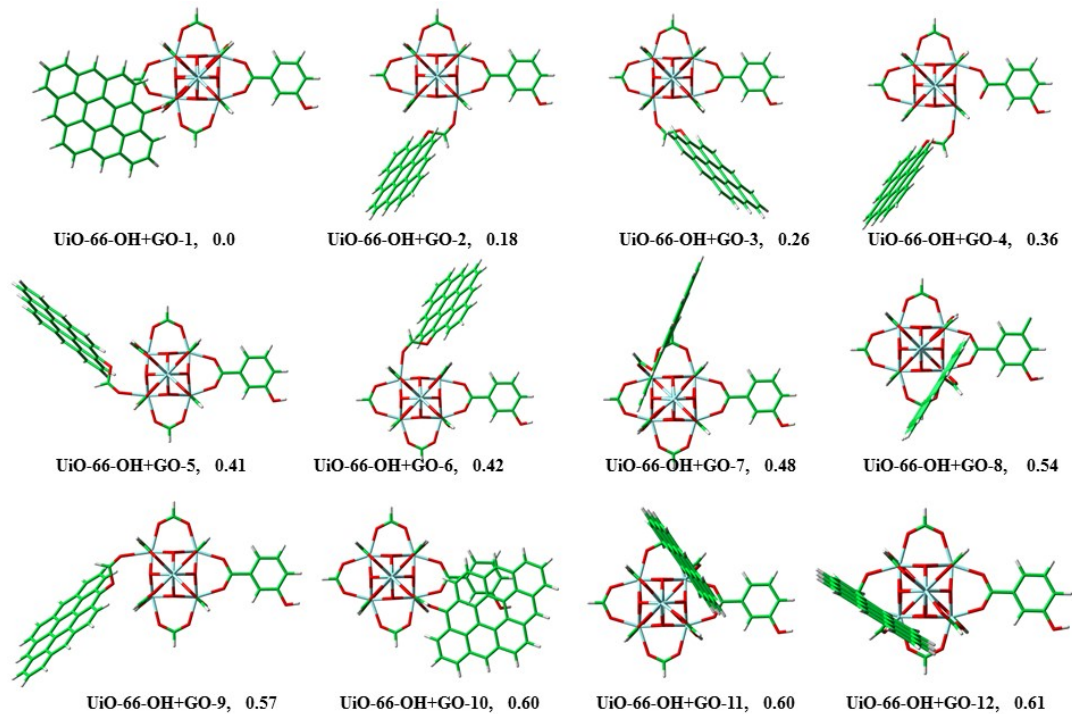
Fig. S16 Optimized adsorption structures of UiO-66-OH toward GO, the relative energies are provided (kcal/mol).

UiO-66-(OH)₂+GO-1, 0.0   UiO-66-(OH)₂+GO-2, 0.40   UiO-66-(OH)₂+GO-3, 1.13   UiO-66-(OH)₂+GO-4, 1.14

UiO-66-(OH)₂+GO-5, 1.21   UiO-66-(OH)₂+GO-6, 1.29   UiO-66-(OH)₂+GO-7, 1.40   UiO-66-(OH)₂+GO-8, 1.46

UiO-66-(OH)₂+GO-9, 1.49   UiO-66-(OH)₂+GO-10, 1.57   UiO-66-(OH)₂+GO-11, 1.61   UiO-66-(OH)₂+GO-12, 1.76
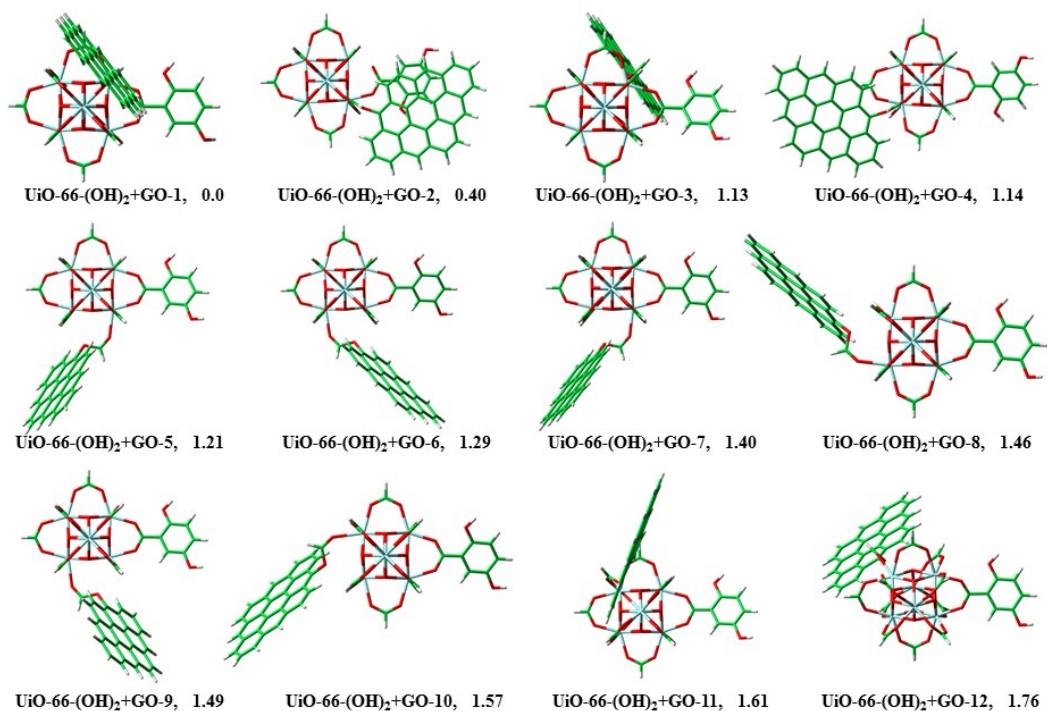
Fig. S17 Optimized adsorption structures of UiO-66-(OH)$_2$ toward GO, the relative energies are provided (kcal/mol).

UiO-66-NH₂+GO-1, 0.0   UiO-66-NH₂+GO-2, 0.39   UiO-66-NH₂+GO-3, 0.42   UiO-66-NH₂+GO-4, 0.44

UiO-66-NH₂+GO-5, 0.46   UiO-66-NH₂+GO-6, 0.49   UiO-66-NH₂+GO-7, 0.50   UiO-66-NH₂+GO-8, 0.55

UiO-66-NH₂+GO-9, 0.60   UiO-66-NH₂+GO-10, 0.67   UiO-66-NH₂+GO-11, 0.71   UiO-66-NH₂+GO-12, 0.73

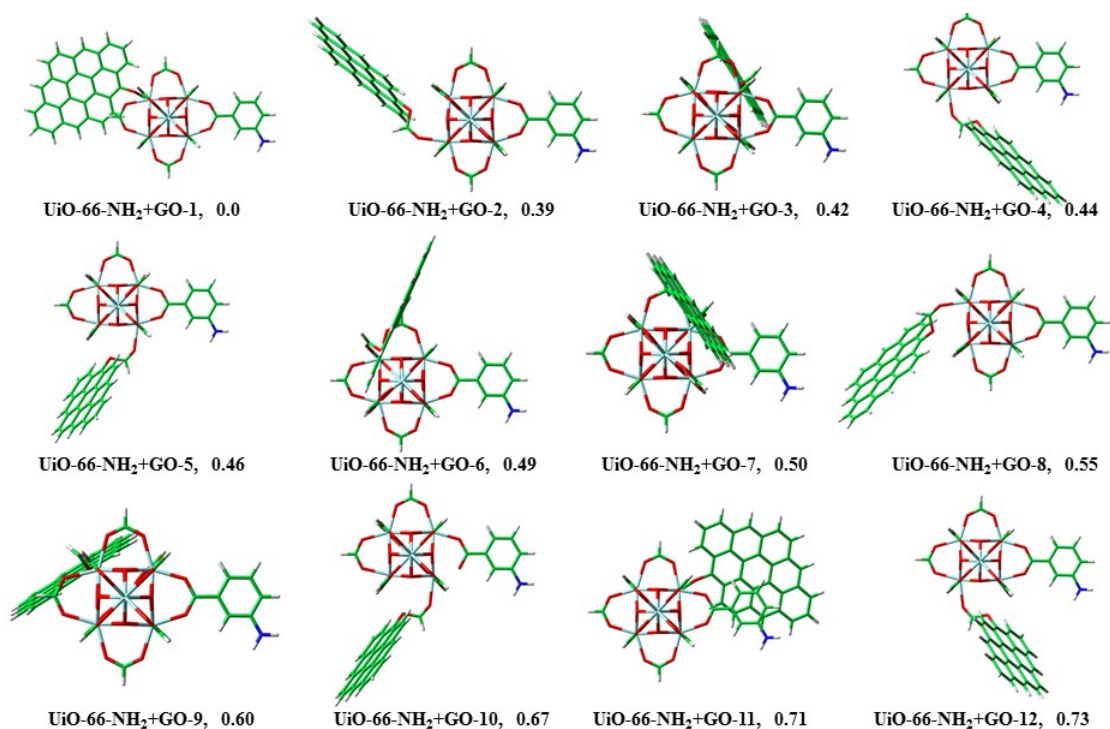**Fig. S18** Optimized adsorption structures of UiO-66-NH$_2$ toward GO, the relative energies are provided (kcal/mol).

Table S1 Experimental parameters for the synthesis of Zr-based MOFs described in this work.

Materials	ZrCl$_4$ (mg)	Ligand (mg)	HCl (mL)	DMF (mL)
UiO-66	125 (0.54 mmol)	123 (0.75 mmol)	1	15
UiO-66-NH$_2$	125 (0.54 mmol)	134 (0.75 mmol)	1	15
UiO-66-OH	125 (0.54 mmol)	135 (0.75 mmol)	1	15
UiO-66-(OH)$_2$	125 (0.54 mmol)	147 (0.75 mmol)	1	15
UiO-67	67 (0.27 mmol)	90 (0.38 mmol)	0.5	15

Table S2 Surface areas and pore volumes of Zr-MOFs.

Materials	BET surface area (m^2/g)	Pore volume (cm^3/g)	Average pore diameter (Å)
UiO-66	1500	0.752	8, 11
UiO-66-NH$_2$	1150	0.858	6, 11
UiO-66-OH	960	0.449	6, 11
UiO-66-(OH)$_2$	540	0.253	5, 11
UiO-67	2450	1.192	11, 23

Table S3 Fitting results of the adsorption isotherms of Zr-based MOFs by Linear model, Freundlich and Langmuir models.

Materials	Linear model			Freundlich model			Langmuir model		
	K (L/g)	Q_l (mg/g)	R^2	K_f $((mg/g)/(mg/L)^n)$	n	R^2	$C_{s\ max}$ (mg/g)	b (L/mg)	R^2
UiO-66	27.233±1.158	9.806±0.337	0.967	28.842±1.765	0.640±0.035	0.969	205.917±25.01	0.145±0.028	0.943
UiO-66-NH$_2$	45.014±1.122	10.918±0.455	0.934	44.157±2.449	0.434±0.033	0.940	135.93±14.49	0.741±0.191	0.877
UiO-67	51.292±1.059	13.409±0.514	0.959	50.431±1.588	0.444±0.017	0.944	143.547±12.76	1.014±0.226	0.924

Table S4 Fitting results of the adsorption isotherms of Zr-based MOFs by Linear model and Freundlich model.

Materials		Linear model			Freundlich model		
		K (L/g)	Q_l (mg/g)	R^2	K_f $((mg/g)/(mg/L)^n)$	n	R^2
UiO-66	Adsorption	27.233±1.158	9.806±0.337	0.967	28.842±1.765	0.640±0.035	0.969
	Desorption	35.316±0.956	13.442±0.514	0.952	33.554±1.428	0.562±0.026	0.965
UiO-66-NH$_2$	Adsorption	45.014±1.122	10.918±0.455	0.934	44.157±2.449	0.434±0.033	0.940
	Desorption	50.040±1.166	16.742±0.692	0.935	49.130±2.521	0.422±0.028	0.936
UiO-67	Adsorption	51.292±1.059	13.409±0.514	0.959	50.431±1.588	0.444±0.017	0.944
	Desorption	52.003±1.456	23.983±0.994	0.954	58.014±3.465	0.318±0.028	0.945

Table S5 Comparison of the aggregation capacities of various coagulates.

Materials	Aggregation capacity (mg/g)	Ref.
Ca/Al-LDH	123	[1]
Al_2O_3	0.59	[2]
quartz sand	0.004	[3]
Geo-Ca	6.06	[4]
C@La-TiO$_2$	383.3	[5]
LDO-Gl	448.3	[6]
Mg/Al/La-CLDHs	558.6	[7]
UiO-67	50.43	This work

Reference

1. J. Wang, X. Wang, L. Tan, Y. Chen, T. Hayat, J. Hu, A. Alsaedi, B. Ahmad, W. Guo and X. Wang, *Chem. Eng. J.*, 2016, **297**, 106-115.

2. X. Ren, J. Li, X. Tan, W. Shi, C. Chen, D. Shao, T. Wen, L. Wang, G. Zhao and G. Sheng, *Environmen. Sci. Technol.*, 2014, **48**, 5493-5500.

3. N. P. Sotirelis and C. V. Chrysikopoulos, *Environ. Sci. Technol.*, 2015, **49**, 13413-13421.

4. J. Zhao, F. Liu, Z. Wang, X. Cao and B. Xing, *Environmen. Sci. Technol.*, 2015, **49**, 2849-2857.

5. J. Wang, Y. Liang, Q. Jin, J. Hou, B. Liu, X. Li, W. Chen, T. Hayat, A. Alsaedi and X. Wang, *ACS Sustain. Chem. Eng.*, 2017, **5**, 5550-5561.

6. Y. Zou, X. Wang, Z. Chen, W. Yao, Y. Ai, Y. Liu, T. Hayat, A. Alsaedi, N. S.

Alharbi and X. Wang, *Environ. Pollut.*, 2016, **219**, 107-117.

7.   J. Wang, Y. Li, W. Chen, J. Peng, J. Hu, Z. Chen, T. Wen, S. Lu, Y. Chen, T.

Hayat, B. Ahmad and X. Wang, *Chem. Eng. J.*, 2017, **309**, 445-453.